Available online at www.sciencedirect.com
ScienceDirect
Journal of Computational Physics 225 (2007) 363–381
JOURNAL OF COMPUTATIONAL PHYSICS
www.elsevier.com/locate/jcp

An adaptive finite element method for magnetohydrodynamics

S. Lankalapalli [a], J.E. Flaherty [b,*], M.S. Shephard [b], H. Strauss [c]

[a] *Third Wave Systems, Minneapolis, MN, United States*
[b] *Scientific Computation Research Center, Rensselaer Polytechnic Institute, Troy, NY 12180-3590, United States*
[c] *Courant Institute of Mathematical Sciences, New York University, NY, United States*

Received 12 September 2005; received in revised form 19 September 2006; accepted 2 December 2006
Available online 30 December 2006

Abstract

We describe a procedure for the adaptive *h*-refinement solution of the incompressible MHD equations in stream function form using a stabilized finite element formulation. The mesh is adapted based on a posteriori spatial error estimates of the magnetic field using both recovery and order extrapolation techniques. The step size for time integration is chosen so that temporal discretization errors are small relative to spatial errors. The adaptive procedure is applied to study singular current sheets in the tilt instability problem of ideal magnetohydrodynamics. Numerical results indicate a more accurate resolution of current sheets with higher-order methods than with piecewise-linear approximations.

Keywords: Adaptive *h*-refinement; Incompressible MHD; Stabilized finite element formulation

1. Introduction

Magnetohydrodynamics (MHD) is the study of electrically conducting fluids in the presence of a magnetic field. Fluid motion in a magnetic field induces electric currents which modify the field, and, at the same time, the flow of electric currents in the magnetic field produces a mechanical force that modifies the fluid motion. This characteristic two way coupling exhibited by the physical system makes MHD both interesting and difficult to study. MHD has applications in plasma physics (fusion power generation, astrophysics, etc.) and the motion of liquid metals.

MHD motion of plasmas tends to develop sharp structures such as nearly discontinuous magnetic fields and sharply localized, intense current sheets. If the resolution is inadequate, the discretization error can cause excess numerical dissipation, magnetic reconnection, and/or spurious oscillations. Therefore, it is important to resolve the solution in the proper areas as the current sheets form and move. To ensure the reliability of the simulation, mesh refinements must be done adaptively since the location of the current sheets evolve with time.

Various approaches have been used to reduce numerical dissipation in computational MHD. These include the use of mixed finite difference and spectral discretizations [4] and finite difference schemes with nonuniform,

* Corresponding author.
E-mail address: flahej@rpi.edu (J.E. Flaherty).

0021-9991/$ - see front matter © 2007 Elsevier Inc. All rights reserved.
doi:10.1016/j.jcp.2006.12.010

cartesian product grids in which intense current sheets are aligned with the grid [2]. Schnack et al. [3] used a finite volume method on unstructured adaptive grids to solve problems with axial symmetry. Friedal et al. [5] used structured adaptive mesh refinement whereas Strauss et al. [1] used a Galerkin finite element method with unstructured adaptive meshes to resolve current sheets in ideal incompressible MHD flows in two dimensions. Strauss et al. [1] used a mesh criterion based on a threshold value for the product of the current density and element area. In order to avoid unnecessary mesh refinement in regions far from the current sheets, the refinement criterion was weighted in terms of the magnetic separatrix. Recently, Jardin [6] used a reduced quintic triangular finite element with C^1 continuity to solve two dimensional, incompressible, resistive MHD equations with no adaptivity.

We develop an adaptive finite element solution procedure on unstructured meshes for incompressible MHD flow problems in streamfunction-vorticity form. The procedure uses a stabilized finite element formulation and adaptive *h*-refinement based on a posteriori temporal and spatial error estimates of the magnetic field. Spatial error estimates based on recovery (the difference between post-processed smoothed finite element solution and the finite element solution) and order extrapolation (the difference between finite element solutions of different polynomial orders) are used to guide mesh adaptivity. Temporal estimates of local discretization errors are obtained from order extrapolation between solutions obtained by backward Euler and trapezoidal rule methods. We use a method-of-lines approach that is designed to maintain (local) time error estimates at a small fraction of the (global) spatial error estimate [7]. The procedure is applied to resolve the singular current sheets that form in the tilt instability [1,26] problem of ideal MHD. By using higher-order extrapolation error estimates, we demonstrate the benefits of using higher-order finite element methods in terms of solution accuracy per unit of computational cost.

In Section 2, we describe the incompressible MHD equations. In Section 3, we outline the stabilized finite element formulation. This is followed by the spatial and time discretization procedure in Section 4. In Section 5, we describe the error estimation and adaptivity procedures. In Section 6, we describe the tilt instability problem and present numerical results. Finally, we summarize our findings and present conclusions in Section 7.

2. Incompressible MHD equations

The incompressible MHD equations consist of the Navier–Stokes equations [17] coupled to Maxwell equations [19] and consist of

$$\frac{\partial \boldsymbol{v}}{\partial} = -(\boldsymbol{v}\cdot\nabla)\boldsymbol{v} + \frac{1}{\rho}(\nabla\times\boldsymbol{B})\times\boldsymbol{B} + \mu\nabla^2\boldsymbol{v}, \tag{2.1}$$

$$\nabla\cdot\boldsymbol{v} = 0, \tag{2.2}$$

$$\frac{\partial \boldsymbol{B}}{\partial} = \nabla\times(\boldsymbol{v}\times\boldsymbol{B}), \tag{2.3}$$

$$\nabla\cdot\boldsymbol{B} = 0, \tag{2.4}$$

where $\boldsymbol{v}$ is the velocity, $\rho = \rho_0$ is the (constant) density, assumed constant, $\boldsymbol{B}$ is the magnetic field and μ is the fluid viscosity. Eq. (2.3) is obtained from Faraday's law after using Ohm's law to write the electric field in terms of the magnetic field [19]. Eq. (2.1) is the Navier–Stokes equation with a Lorentz force as the body force. Eqs. (2.2) and (2.4) express the incompressibility condition on the velocity and magnetic fields, respectively. The above equations model the case of ideal MHD since the resistivity term in Ohm's law is neglected.

The equations can be made dimensionless, by normalizing B to a reference magnetic field strength B_0, ρ to ρ_0, v to the Alfven velocity $_{\mathrm{A}} = B_0/\sqrt{\rho_0}$, length to l, and time to the Alfven time, $\mathrm{l}/v_{\mathrm{A}}$. To enforce the incompressibility conditions on the velocity and magnetic fields, we introduce the stream functions

$$\boldsymbol{v} = \left(\frac{\partial\phi}{\partial\kappa}, -\frac{\partial\phi}{\partial}\right), \tag{2.5}$$

$$\boldsymbol{B} = \left(\frac{\partial\psi}{\partial\kappa}, -\frac{\partial\psi}{\partial}\right), \tag{2.6}$$

where ϕ and ψ are the velocity flux and magnetic flux, respectively. Substituting Eqs. (2.5) and (2.6) into Eqs. (2.3) and (2.4) and following the symmetrization procedure of Strauss et al. [1], we obtain the following stream function formulation:

$$\frac{\partial \Omega}{\partial} + [\Omega, \phi] = [C, \psi] + \mu \nabla^2 \Omega, \tag{2.7}$$

$$\frac{\partial C}{\partial} + [C, \phi] = [\Omega, \psi] + 2\left[\frac{\partial \phi}{\partial}, \frac{\partial \psi}{\partial}\right] + 2\left[\frac{\partial \phi}{\partial \kappa}, \frac{\partial \psi}{\partial \kappa}\right], \tag{2.8}$$

$$\nabla^2 \phi = \Omega, \tag{2.9}$$

$$\nabla^2 \psi = C, \tag{2.10}$$

where Ω is the vorticity, C is the current density and

$$[\ ,\ ] = \frac{\partial}{\partial}\frac{\partial}{\partial \kappa} - \frac{\partial}{\partial \kappa}\frac{\partial}{\partial}$$

is the Poisson bracket. The equations are symmetric in the sense that the source functions C and Ω are time advanced, and fluxes ϕ and Ω are obtained at each time step by solving Poisson problems.

3. Stabilized finite element formulation

Eqs. (2.7)–(2.10) provide a formidable coupled and nonlinear system. In addition, Eqs. (2.7) and (2.8) introduce advection into the problem, since gradients of ϕ in the Poisson brackets provide advective velocities for Ω and C in (2.7) and (2.8), respectively.

It is well known that standard Galerkin finite element methods fail for advection and advection dominated advection-diffusion problems [8,10,11]. Spurious oscillations occur when solutions in layers are not adequately resolved. Several remedies that suppress the oscillations by adding diffusion have been proposed. The methods may be classified into quadrature based methods [12,11] and Galerkin least squares stabilization methods [13,15]. The Galerkin least-squares method consists of adding diffusion in a least-squares form of the residual to the Galerkin method. Quadrature based methods add diffusion by using specialized quadrature rules when evaluating element contributions.

We use the Streamline Upwind Petrov–Galerkin (SUPG) stabilized finite element method which was first proposed by Hughes et al. [8,9] to solve Eqs. (2.7) and (2.8). The SUPG method is a special case of the Galerkin least-squares method with the stabilization terms consisting of only the advective operator multiplying the residual of the strong form of the problem. To begin, we construct a Galerkin form of Eqs. (2.7)–(2.10) by multiplying each by test functions $w_i, \boldsymbol{h}$ $= 1, 2, 3, 4$, integrating over the domain $\mathscr{R}$, and integrating the diffusive terms by parts to obtain

$$B_1(\Omega, \ _1) \equiv \left(\frac{\partial \Omega}{\partial} + [\Omega, \phi] - [C, \psi], \ _1\right) + \mu(\nabla \Omega, \nabla \ _1) = 0, \tag{3.1}$$

$$B_2(C, \ _2) \equiv \left(\frac{\partial C}{\partial}, \ _2\right) + \left([C, \phi] - [\Omega, \psi] - 2\left[\frac{\partial \phi}{\partial}, \frac{\partial \psi}{\partial}\right] - 2\left[\frac{\partial \phi}{\partial \kappa}, \frac{\partial \psi}{\partial \kappa}\right], \ _2\right) = 0, \tag{3.2}$$

$$-(\nabla \phi, \nabla \ _3) = (\Omega, \ _3), \tag{3.3}$$

$$-(\nabla \psi, \nabla \ _4) = (C, \ _4), \tag{3.4}$$

where

$$(\ ,\ ) = \int_{\mathscr{R}} \ \mathrm{d}$$

and homogeneous Dirichlet boundary conditions were assumed for simplicity.

The SUPG stabilized weak form of the problem is obtained by replacing Eqs. (3.1) and (3.2) by

$$B_1(\Omega, \ _1) + \sum_{\mathrm{T} \in \mathscr{T}} \left(\frac{\partial \Omega}{\partial} + [\Omega, \phi] - [C, \psi] - \mu \nabla^2 \Omega, \tau[\ _1, \phi]\right) = 0, \tag{3.5}$$

$$B_2(C, \quad _2) + \sum_{T\in\mathscr{T}} \left(\frac{\partial C}{\partial} + [C, \phi] - [\Omega, \psi] - 2\left[\frac{\partial \phi}{\partial}, \frac{\partial \psi}{\partial}\right] - 2\left[\frac{\partial \phi}{\partial \kappa}, \frac{\partial \psi}{\partial \kappa}\right], \tau[\quad _2, \phi] \right) = 0, \tag{3.6}$$

where $\mathscr{T}$ is a partition of the domain into a mesh of non-overlapping elements. The stabilization terms are an element-level inner product of the residual of the strong form of the equation and the advective portion of the operator acting on the test function weighted by a stabilization parameter τ. Several definitions of the stabilization parameter τ have been proposed and we use one suggested by Tezduyar et al. [14]

$$\tau = \left[\frac{1}{\tau_1^2} + \frac{1}{\tau_2^2}\right]^{-\frac{1}{2}}, \quad \tau_1 = \frac{\quad _e}{2|\boldsymbol{a}|} \max(\quad , 1), \quad \tau_2 = \frac{\Delta}{2}, \tag{3.7}$$

$$= \frac{|\boldsymbol{a}| \quad _e}{2\mu}, \quad \quad = \min\left(\frac{1}{3}, 2C \quad\right), \tag{3.8}$$

where τ_1 is a parameter for the advection dominated case [15] and τ_2 is a parameter for transient dominated case defined in terms of the time step Δt. Additionally, Pe is the cell Peclet number, h_e represents a suitably chosen element diameter (maximum edge length in our implementation),

$$\boldsymbol{a} = \left[\frac{\partial \phi}{\partial} \quad \frac{\partial \phi}{\partial \kappa}\right]^T \tag{3.9}$$

is the advective velocity and C_k is a constant that depends on the polynomial degree of the basis and represents a modification of τ_1. The existence of such a constant follows from inverse estimates [16] and Harari et al. [20] provide some guidance on how to choose it as a function of polynomial degree. In our numerical simulations, we simply choose $m_k = 1/3$.

The addition of stabilization terms to Eqs. (3.1) and (3.2) is equivalent to using discontinuous Petrov–Galerkin weighting functions $\quad _1'$ and $\quad _2'$ that perturb the Galerkin weight functions by

$$\quad _1' = (\quad _1 + \quad _1), \quad \quad _2' = (\quad _2 + \quad _2), \tag{3.10}$$

where $\quad _1 = \tau[\quad _1, \phi]$ and $\quad _2 = \tau[\quad _2, \phi]$ are the perturbations. With this, the weak form of the system of equations with SUPG stabilization may be concisely written as

$$\left(\frac{\partial \Omega}{\partial} + [\Omega, \phi] - [C, \psi], \quad _1'\right) + \mu(\nabla\Omega, \nabla \quad _1) - \mu(\nabla^2\Omega, \quad _1) = 0, \tag{3.11}$$

$$\left(\frac{\partial C}{\partial}, \quad _2'\right) + \left([C, \phi] - [\Omega, \psi] - 2\left[\frac{\partial \phi}{\partial}, \frac{\partial \psi}{\partial}\right] - 2\left[\frac{\partial \phi}{\partial \kappa}, \frac{\partial \psi}{\partial \kappa}\right], \quad _2'\right) = 0, \tag{3.12}$$

$$-(\nabla\phi, \nabla \quad _3) = (\Omega, \quad _3), \tag{3.13}$$

$$-(\nabla\psi, \nabla \quad _4) = (C, \quad _4). \tag{3.14}$$

4. Discretization

For the spatial discretization, we partition the problem domain $\mathscr{R}$ into a mesh of non-overlapping elements $\mathscr{T}$, and define basis functions $\lambda_{\quad}(\mathbf{x})$, $\quad = 1, 2, \ldots, \quad$, where $\mathbf{x}$ is a vector of spatial coordinates and N is the dimension of the approximating space. We use a Lagrange basis [18] on a two-dimensional mesh of triangular elements. We obtain a finite element version of Eqs. (3.11)–(3.14) by approximating the MHD variables ϕ, Ω, ψ and C as linear combinations of the basis functions as

$$\begin{bmatrix} \Omega \\ C \\ \phi \\ \psi \end{bmatrix} (\mathbf{x}, \quad) = \sum_{\quad=1} \begin{bmatrix} \Omega \\ C \\ \phi \\ \psi \end{bmatrix} (\quad) \lambda_{\quad}(\mathbf{x}). \tag{4.1}$$

Substituting Eq. (4.1) into Eqs. (3.11)–(3.14), testing with each of the basis functions λ_i, $i = 1, 2, \ldots, N$, and integrating over the mesh $\mathscr{T}$ results in the following algebraic system:

$$\mathbf{M}\cdot\frac{\partial\overline{\mathbf{\Omega}}}{\partial}-\mathbf{P}:\overline{\mathbf{\Phi}\mathbf{\Omega}}-\mathbf{P}:\overline{\mathbf{C}\mathbf{\Psi}}+\mu\mathbf{S}\cdot\overline{\mathbf{\Omega}}=0, \tag{4.2}$$

$$\mathbf{M}\cdot\frac{\partial\overline{\mathbf{C}}}{\partial}+\mathbf{P}:\overline{\mathbf{C}\mathbf{\Phi}}-\mathbf{P}:\overline{\mathbf{\Omega}\mathbf{\Psi}}-2(\mathbf{Q}:\overline{\mathbf{\Phi}\mathbf{\Psi}})-2(\mathbf{R}:\overline{\mathbf{\Phi}\mathbf{\Psi}})=0, \tag{4.3}$$

$$\mathbf{S}\cdot\overline{\mathbf{\Phi}}=\mathbf{M}\cdot\overline{\mathbf{\Omega}}, \tag{4.4}$$

$$\mathbf{S}\cdot\overline{\mathbf{\Psi}}=\mathbf{M}\cdot\overline{\mathbf{C}}, \tag{4.5}$$

where $\overline{\mathbf{\Omega}}$, $\overline{\mathbf{C}}$, $\overline{\mathbf{\Phi}}$ and $\overline{\mathbf{\Psi}}$ are vectors of Galerkin coefficients, $\mathbf{M}$ is the mass matrix, $\mathbf{S}$ is the stiffness matrix, $\mathbf{P}$, $\mathbf{Q}$ and $\mathbf{R}$ are discrete Poisson bracket tensors. Additionally,

$$(\mathbf{M}\cdot\overline{\mathbf{C}})_{\hbar}=\sum_{=1}\ {}_{\hbar}C\ , \tag{4.6}$$

$$(\mathbf{P}:\overline{\mathbf{\Phi}\mathbf{\Omega}})_{\hbar}=\sum_{,=1}\ {}_{\hbar\cdot}\phi\ \Omega_{\cdot}\ , \tag{4.7}$$

$$(\mathbf{Q}:\overline{\mathbf{\Phi}\mathbf{\Psi}})_{\hbar}=\sum_{,=1}\ {}_{\hbar\cdot}\phi\ \psi_{\cdot}\ , \tag{4.8}$$

$$(\mathbf{R}:\overline{\mathbf{\Phi}},\overline{\mathbf{\Psi}})_{\hbar}=\sum_{,=1}\ {}_{\hbar\cdot}\phi\ \psi_{\cdot}\ , \tag{4.9}$$

where

$${}_{\hbar}=\int_{\mathscr{T}_{\cdot}}(\lambda_{\hbar}+\tau[\lambda_{\hbar},\phi])\lambda\ \mathrm{d}\quad , \tag{4.10}$$

$${}_{\hbar}=\int_{\mathscr{T}_{\cdot}}(\nabla\lambda_{\hbar}\nabla\lambda\ -\tau[\lambda_{\hbar},\phi]\Delta\lambda\ )\mathrm{d}\quad , \tag{4.11}$$

$${}_{\hbar\cdot}=\int_{\mathscr{T}_{\cdot}}(\lambda_{\hbar}+\tau[\lambda_{\hbar},\phi])[\lambda\ ,\lambda_{\cdot}\ ]\mathrm{d}\quad , \tag{4.12}$$

$${}_{\hbar\cdot}=\int_{\mathscr{T}_{\cdot}}(\lambda_{\hbar}+\tau[\lambda_{\hbar},\phi])[\lambda\ ,\ ,\lambda_{\cdot}\ ,\ ]\mathrm{d}\quad , \tag{4.13}$$

$${}_{\hbar\cdot}=\int_{\mathscr{T}_{\cdot}}(\lambda_{\hbar}+\tau[\lambda_{\hbar},\phi])[\lambda\ ,_{\kappa},\lambda_{\cdot}\ ,_{\kappa}]\mathrm{d}\quad . \tag{4.14}$$

The second derivatives of basis functions in the Poisson brackets are computed in our implementation by differentiating the piecewise continuous global projection of the derivatives of the basis functions.

The semi-discrete Eqs. (4.2)–(4.5) are linearized and decoupled by retarding variables as follows:

$$\mathbf{M}\cdot\frac{\partial\overline{\mathbf{\Omega}}^{\ +1}}{\partial}-\mathbf{P}:\overline{\mathbf{\Phi}}\ \overline{\mathbf{\Omega}}^{\ +1}-\mathbf{P}:\overline{\mathbf{C}}\ \overline{\mathbf{\Psi}}\ +\mu\mathbf{S}\cdot\overline{\mathbf{\Omega}}^{\ +1}=0, \tag{4.15}$$

$$\mathbf{M}\cdot\frac{\partial\overline{\mathbf{C}}^{\ +1}}{\partial}+\mathbf{P}:\overline{\mathbf{C}}^{\ +1}\overline{\mathbf{\Phi}}\ -\mathbf{P}:\overline{\mathbf{\Omega}}^{\ +1}\overline{\mathbf{\Psi}}\ -2(\mathbf{Q}:\overline{\mathbf{\Phi}}\ \overline{\mathbf{\Psi}}\ )-2(\mathbf{R}:\overline{\mathbf{\Phi}}\ \overline{\mathbf{\Psi}}\ )=0, \tag{4.16}$$

$$\mathbf{S}\cdot\overline{\mathbf{\Phi}}^{\ +1}=\mathbf{M}\cdot\overline{\mathbf{\Omega}}^{\ +1}, \tag{4.17}$$

$$\mathbf{S}\cdot\overline{\mathbf{\Psi}}^{\ +1}=\mathbf{M}\cdot\overline{\mathbf{C}}^{\ +1},\quad .\ =0,1,\ldots, \tag{4.18}$$

where the superscript k indicates an iteration index. We use the backward Euler method to discretize Eqs. (4.15) and (4.16) in time to get

$$\mathbf{M}\cdot\overline{\mathbf{\Omega}}_{\ +1}^{\ +1}=\mathbf{M}\cdot\overline{\mathbf{\Omega}}_{\ }^{\ }+\Delta\ \mathbf{F}(\overline{\mathbf{\Omega}}_{\ +1}^{\ +1},\overline{\mathbf{C}}_{\ +1}^{\ },\overline{\mathbf{\Phi}}_{\ +1}^{\ },\overline{\mathbf{\Psi}}_{\ +1}^{\ }), \tag{4.19}$$

$$\mathbf{M}\cdot\overline{\mathbf{C}}_{\ +1}^{\ +1}=\mathbf{M}\cdot\overline{\mathbf{C}}_{\ }^{\ }+\Delta\ \mathbf{G}(\overline{\mathbf{\Omega}}_{\ +1}^{\ +1},\overline{\mathbf{C}}_{\ +1}^{\ +1},\overline{\mathbf{\Phi}}_{\ +1}^{\ },\overline{\mathbf{\Psi}}_{\ +1}^{\ }), \tag{4.20}$$

$$\mathbf{S}\cdot\overline{\mathbf{\Phi}}_{\ +1}^{\ +1}=\mathbf{M}\cdot\overline{\mathbf{\Omega}}_{\ +1}^{\ +1}, \tag{4.21}$$

$$\mathbf{S}\cdot\overline{\mathbf{\Psi}}_{\ +1}^{\ +1}=\mathbf{M}\cdot\overline{\mathbf{C}}_{\ +1}^{\ +1}, \tag{4.22}$$

where,

$$\mathbf{F}(\overline{\mathbf{\Omega}}, \overline{\mathbf{C}}, \overline{\mathbf{\Phi}}, \overline{\mathbf{\Psi}}) = \mathbf{P} : \overline{\mathbf{\Phi}}\overline{\mathbf{\Omega}} + \mathbf{P} : \overline{\mathbf{C}}\overline{\mathbf{\Psi}} - \mu\mathbf{S} \cdot \overline{\mathbf{\Omega}}, \tag{4.23}$$

$$\mathbf{G}(\overline{\mathbf{\Omega}}, \overline{\mathbf{C}}, \overline{\mathbf{\Phi}}, \overline{\mathbf{\Psi}}) = -\mathbf{P} : \overline{\mathbf{C}}\overline{\mathbf{\Phi}} + \mathbf{P} : \overline{\mathbf{\Omega}}\overline{\mathbf{\Psi}} + 2(\mathbf{Q} : \overline{\mathbf{\Phi}}\overline{\mathbf{\Psi}}) + 2(\mathbf{R} : \overline{\mathbf{\Phi}}\overline{\mathbf{\Psi}}), \tag{4.24}$$

the subscript n represents time. For each time step, we solve Eqs. (4.19)–(4.22) in sequence and repeat the iteration for five times before checking for convergence with a tolerance of $1.0e-4$. A preconditioned *gmres* iterative solver was used to solve the system of equations. If there is no convergence, we halve the time step and restart the procedure.

We compute a second solution by repeating the above procedure, using trapezoidal rule integration for the time discretization of Eqs. (4.15) and (4.16) to get

$$\mathbf{M} \cdot \overline{\mathbf{\Omega}}^{n+1} = \mathbf{M} \cdot \overline{\mathbf{\Omega}}^{n} + \frac{\Delta}{2}\left(\mathbf{F}(\overline{\mathbf{\Omega}}^{n+1}, \overline{\mathbf{C}}^{n+1}, \overline{\mathbf{\Phi}}^{n+1}, \overline{\mathbf{\Psi}}^{n+1}) + \mathbf{F}(\overline{\mathbf{\Omega}}^{n}, \overline{\mathbf{C}}^{n}, \overline{\mathbf{\Phi}}^{n}, \overline{\mathbf{\Psi}}^{n})\right), \tag{4.25}$$

$$\mathbf{M} \cdot \overline{\mathbf{C}}^{n+1} = \mathbf{M} \cdot \overline{\mathbf{C}}^{n} + \frac{\Delta}{2}\left(\mathbf{G}(\overline{\mathbf{\Omega}}^{n+1}, \overline{\mathbf{C}}^{n+1}, \overline{\mathbf{\Phi}}^{n+1}, \overline{\mathbf{\Psi}}^{n+1}) + \mathbf{G}(\overline{\mathbf{\Omega}}^{n}, \overline{\mathbf{C}}^{n}, \overline{\mathbf{\Phi}}^{n}, \overline{\mathbf{\Psi}}^{n})\right), \tag{4.26}$$

$$\mathbf{S} \cdot \overline{\mathbf{\Phi}}^{n+1} = \mathbf{M} \cdot \overline{\mathbf{\Omega}}^{n+1}, \tag{4.27}$$

$$\mathbf{S} \cdot \overline{\mathbf{\Psi}}^{n+1} = \mathbf{M} \cdot \overline{\mathbf{C}}^{n+1}. \tag{4.28}$$

We use the Euler solution for $\overline{\mathbf{\Omega}}^{0}_{n+1}$, $\overline{\mathbf{C}}^{0}_{n+1}$, $\overline{\mathbf{\Phi}}^{0}_{n+1}$, $\overline{\mathbf{\Psi}}^{0}_{n+1}$ and solve Eqs. (4.25) and (4.26) in sequence for a fixed number of iterations. The computed trapezoidal solution is of higher order and is used to estimate the time discretization error as described in Section 5.1.

5. Error estimation and adaptivity

We use a posteriori estimates of the spatial and temporal discretization errors to guide mesh adaptivity in space and step size selection in time. We use a method-of-lines approach that is designed to maintain (local) time errors at a small fraction of the (global) spatial error estimate. At the end of every time step, we adapt the mesh based on the computed spatial error estimates and a specified global spatial error tolerance η_{tol}.

Spatial error estimate on the magnetic field is used since the developed method is applied to resolve current sheets in Section 6. Since the current sheets form at the intersection of oppositely directed magnetic field lines, accurate resolution of the magnetic field is expected to result in better resolution of current sheets. In the literature, other criteria have been used to trigger adaptivity for the current sheet problem. These include a criterion based on current density and element area by Strauss et al. [1] and another based on the global maximum of current density and vorticity by Friedal et al. [5].

5.1. Temporal error estimate

An estimate of the local discretization error is obtained using order extrapolation between solutions obtained by backward Euler and trapezoidal rule integration. In order to describe the procedure, let $U(t_n)$ be the solution of the spatially-discrete finite element Eqs. (4.2)–(4.5) with exact time integration on $[t_{n-1}, t_n]$. Let $\phi^1(t_n)$ and $\phi^2(t_n)$ be the backward Euler and trapezoidal rule solutions, respectively. Then, the local time discretization error $\tau(t_n)$ of the backward Euler solution can be bounded as

$$\tau(t_n) = \phi(t_n) - \phi^1(t_n) = [\phi(t_n) - \phi^2(t_n)] + [\phi^2(t_n) - \phi^1(t_n)]. \tag{5.1}$$

Since the leading term on the right is $O(\Delta t_n^3)$ and the second is $O(\Delta t_n^2)$, we have

$$\tau(t_n) = [\phi^2(t_n) - \phi^1(t_n)] + O(\Delta t_n^3), \tag{5.2}$$

where Δt_n is the time step. This estimate of the local error can be used to adjust future time steps to maintain the local error at a small fraction of the total discretization error tolerance η_{tol}. The local error satisfies

$$\tau(t_n) = C_n \Delta t_n^2 + O(\Delta t_n^3), \tag{5.3}$$

where C_n is proportional to a second time derivative of the solution. Using the leading terms of Eqs. (5.2) and (5.3), we find the approximation

$$C_{n} \approx \frac{{}^{2}(\zeta_{n}) - {}^{1}(\zeta_{n})}{\Delta_{n}^{2}}. \tag{5.4}$$

The next time step Δ_{n+1} should satisfy

$$\alpha\eta_{\mathrm{tol}} = C_{n+1}\Delta_{n+1}^{2} \tag{5.5}$$

assuming that the solution remains smooth $C_{n+1} = C_{n} + \mathrm{O}(\Delta_{n+1})$ or, to leading order, $C_{n+1} \approx C_{n}$. Thus, using Eq. (5.4) we find the recommended time step as

$$\Delta_{n+1} = \left[\frac{\alpha\eta_{\mathrm{tol}}(\Delta_{n})^{2}}{|{}^{2} - {}^{1}|}\right]^{\frac{1}{2}}. \tag{5.6}$$

5.2. Spatial error estimates

We obtain estimates of the spatial error by using the relatively standard a posteriori error estimation techniques [21,22] of recovery and extrapolation. In recovery-based error estimation, a smoothed flux is computed by post processing the finite element solution and an error estimate is obtained from the difference between the smoothed and original fluxes. This method was proposed by Zienkiewicz and Zhu [23] (commonly referred to as Z^2 estimator) in the context of linear elliptic problems. To define the error estimate, as before, let ${}^{1}(\zeta_{n})$ be the backward Euler solution and let $\sigma({}^{1}(\zeta_{n}))$ be the computed flux on which an error estimate is to be obtained. Then, the error estimate on a element $\mathrm{T} \in \mathscr{T}$, $\eta_{\mathrm{T}}^{\mathrm{Z}}$, is given by

$$\eta_{\mathrm{T}}^{\mathrm{Z}} = \sigma_{\mathrm{T}}({}^{1}(\zeta_{n})) - \sigma_{\mathrm{T}}^{*}({}^{1}(\zeta_{n})), \tag{5.7}$$

where $\sigma_{\mathrm{T}}^{*}({}^{1}(\zeta_{n}))$ is the flux recovered using the *superconvergent patch recovery* procedure outlined in [23].

An extrapolation error estimate is obtained by taking the difference between the fluxes computed from finite element solutions obtained with different meshes (*h-refinement*) or different orders (*p-refinement*). We use *p-refinement* where the error estimate on an element T, denoted by η_{T}, is obtained as

$$\eta_{\mathrm{T}} = \sigma_{\mathrm{T}}^{+1}({}^{2}(\zeta_{n})) - \sigma_{\mathrm{T}}({}^{2}(\zeta_{n})), \tag{5.8}$$

where, $\sigma_{\mathrm{T}}^{+1}({}^{2}(\zeta_{n}))$ and $\sigma_{\mathrm{T}}({}^{2}(\zeta_{n}))$ are the fluxes computed from trapezoidal solutions at time t_n with spatial order approximations $p+1$ and p, respectively.

The Z^2 estimator is simple to implement and has the additional advantage of having low computational cost. On the other hand, the extrapolation error estimator is computationally expensive due to the necessity of computating two solutions. The computational cost may be reduced by using a hierarchical embedded scheme where computations needed for the lower order method are also needed for the higher order method and, hence, need not be repeated. An advantage of *p*-refinement that is used herein is higher-order solutions are readily available. In our computations, we propagate the higher-order solution by local extrapolation [24] at every time step.

5.3. Mesh adaptivity and solution transfer

After every time step, based on the computed spatial error estimates and a specified global error tolerance η_{tol} we use a mesh optimization procedure [25] to compute the size of elements in the new mesh. The procedure consists of computing a size multiplication factor r_i for element $i = 1, 2, \ldots, N_{\mathrm{el}}$ by solving a minimization problem to determine the optimal number of elements to meet a permitted error norm $\|\ \|$. The element size is specified by its maximum edge length. First, $\|\ (\zeta_{n})\|$ is determined from η_{tol} as

$$\|\ \| = \eta_{\mathrm{tol}}\|\ {}^{1}(\zeta_{n})\|. \tag{5.9}$$

Then, the new element size $h_{\mathrm{new}}[\,]$ is obtained in terms of the old element size $h_{\mathrm{old}}[\,]$ by

$$h_{\mathrm{new}}[\,] = \rho_{h} \cdot h_{\mathrm{old}}[\,], \tag{5.10}$$

where

$$\rho_h = \frac{\eta_h^{\frac{-2}{2+d}} \| \ \|^{1/}}{\left[\sum_{h=1}^{\text{el}} \eta_h^{\frac{2}{2+d}}\right]^{\frac{1}{2}}}, \tag{5.11}$$

η_i is the error estimate for the element i, N_{el} is the total number of elements, p is the polynomial order of the solution and d is the dimension of the problem.

The mesh is adapted using the mesh modification procedures developed by Li et al. [28,29]. This requires the specification of a mesh metric field to define the desired element size and shape distribution from the computed $_{\text{new}}[\,]_h$, $i = 1, 2, \ldots, N_{\text{el}}$. The mesh is then adapted to satisfy the prescribed metric field by the processes of refinement, coarsening and re-alignment.

After mesh adaptation, the finite element solution is transferred to the new mesh from the old mesh by solving the L^2 projection

$$(\ ^1_{\text{new}}(\ )_\eta, \ ) = (\ ^1(\ )_\eta, \ ), \tag{5.12}$$

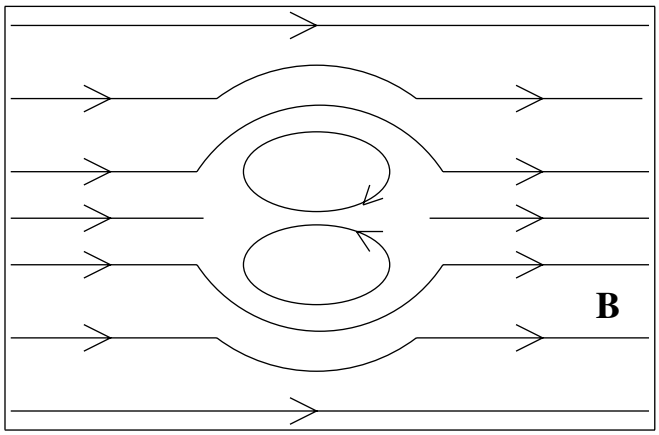

Fig. 1. Tilt instability: initial magnetic field.

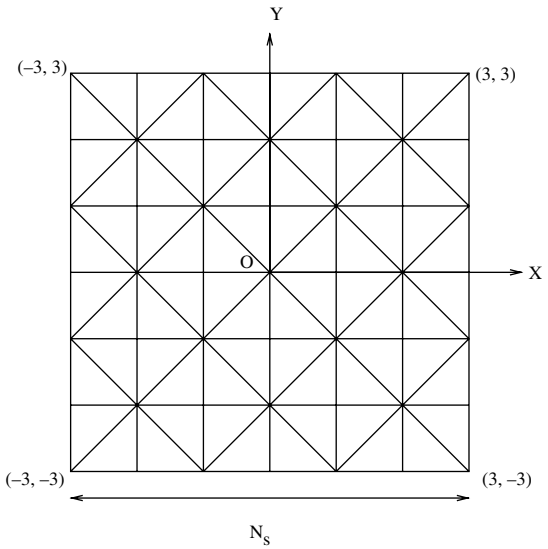

Fig. 2. Uniform mesh of $_s \times \ _s$ squares split into triangles.

where $^{1}_{\text{new}}(\,_{\eta})$ is the solution on the new mesh and w is a weight function. The solution transfer operation is done locally and only in regions where the mesh has been modified.

6. Tilt instability

The tilt instability problem has been studied by Strauss et al. [1] for the incompressible case and by Richard et al. [26] for the compressible case. The initial equilibrium consists of two oppositely directed currents embedded in a constant magnetic field. As a result, there are two adjacent sets of closed magnetic field line loops (Fig. 1) or vortices associated with the currents. The corresponding initial magnetic flux ψ_0 in polar (r,θ) coordinates is given by

$$\psi_0 = \begin{cases} J_1(\,_{\rho})\cos\theta, & \text{if } _{\rho} < 1, \\ (_{\rho} - 1/_{\rho})\cos\theta, & \text{if } _{\rho} \geqslant 1, \end{cases} \tag{6.1}$$

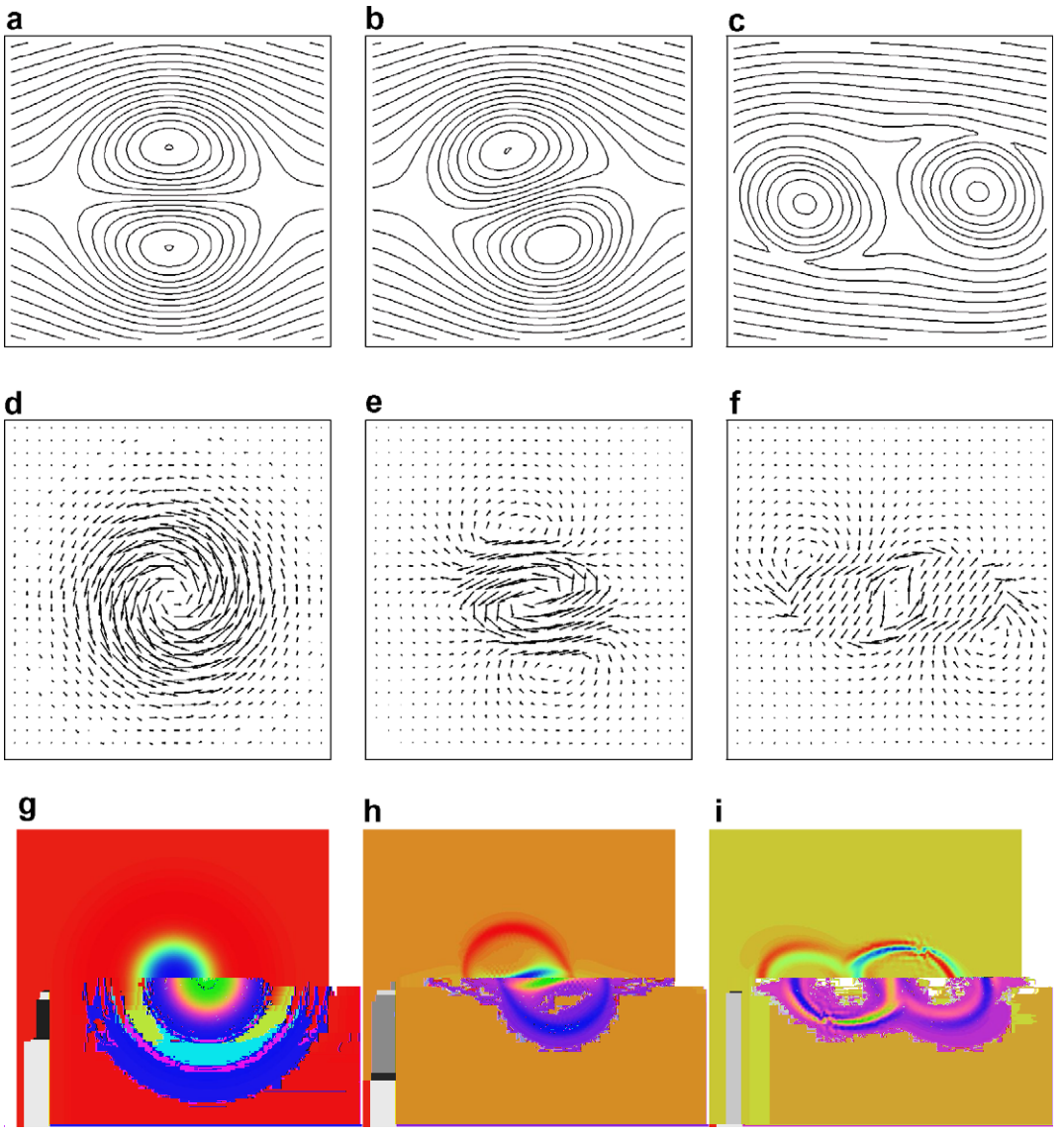

Fig. 3. Magnetic flux (top), velocity field (center) and vorticity (bottom) on a uniform mesh of 32,768 triangles with $p = 1$ at $t = 0$, 5, 6.6. Magnetic flux (ψ): (a) $t = 0$, (b) $t = 5.0$, (c) $t = 6.6$. Velocity ($\boldsymbol{v}$): (d) $t = 0$, (e) $t = 5.0$, (f) $t = 6.6$. Vorticity (Ω): (g) $t = 0$, (h) $t = 5.0$, (i) $t = 6.6$.

where, $= 2/(. J_0(.))$, J_0 and J_1 are Bessel functions of the first kind of order zero and one, respectively, and k is the first root of J_1.

The antiparallel currents repel each other and are prevented from being expelled by the surrounding magnetic field. The resulting initial equilibrium is unstable. When perturbed, the magnetic vortices turn, align horizontally and get expelled from the region. As the vortices align horizontally, intense current gradients (known

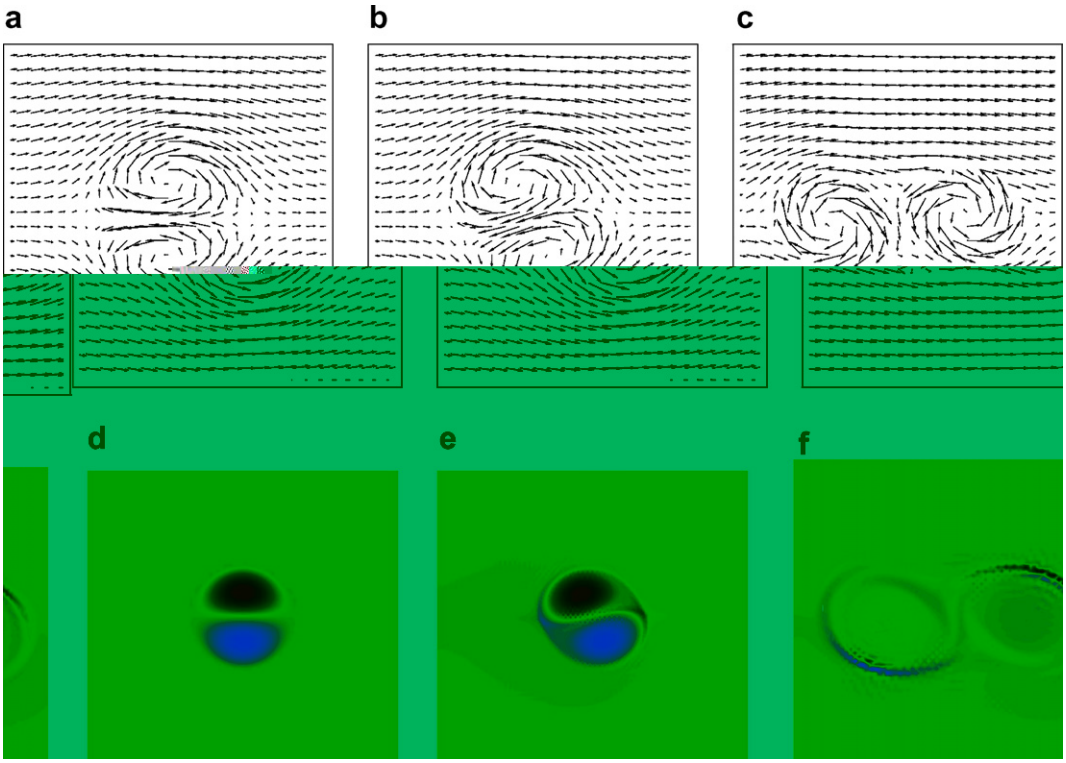

Fig. 4. Magnetic field (top) and current density (bottom) on a uniform mesh of 32,768 triangles with $p = 1$ at $t = 0$, 5, 6.6. Magnetic field (B): (a) $t = 0$, (b) $t = 5.0$, (c) $t = 6.6$. Current density (C): (d) $t = 0$, (e) $t = 5.0$, (f) $t = 6.6$.

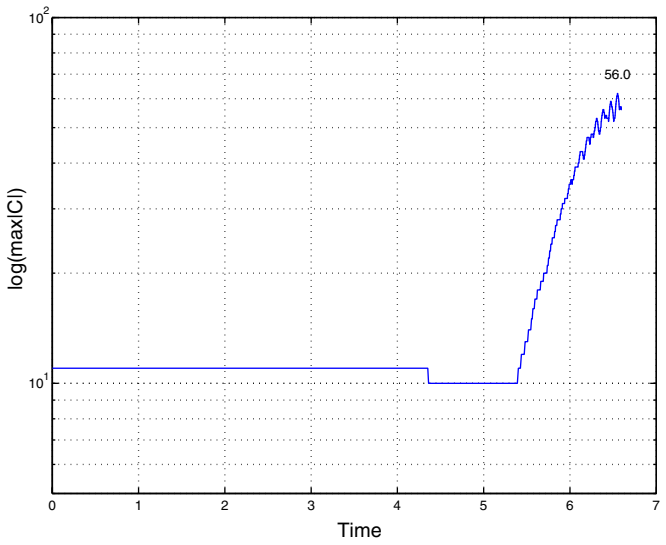

Fig. 5. Peak current density as a function of time on a mesh of 32,768 triangles with $p = 1$.

as current sheets) form at the leading edges of the vortices. Additionally, the kinetic energy grows like $e^{\gamma t}$ for some rate γ.

We used the adaptive methods described in Section 5 to simulate the tilt instability. The software was implemented in Trellis [27], an object oriented framework. Trellis provides various tools to specify the weak form of the problem, perform time integration, error estimation and mesh adaptivity. All simulations were done on a square 6×6 domain that is discretized into a mesh of triangular elements. Initial conditions are

$$\begin{aligned} \Omega(\ ,\kappa,0) &= \nabla^2\phi_0, \\ C(\ ,\kappa,0) &= \nabla^2\psi_0, \end{aligned} \tag{6.2}$$

where the perturbed initial velocity flux,

$$\phi_0(\ ,\kappa,0) = \epsilon e^{-(\ ^2+\kappa^2)}, \tag{6.3}$$

with ϵ being the perturbation magnitude. Boundary conditions are

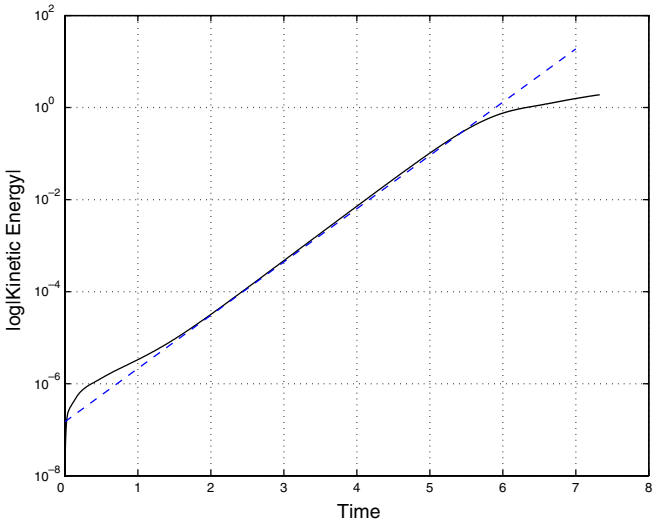

Fig. 6. Estimation of growth rate of kinetic energy by a least squares fit.

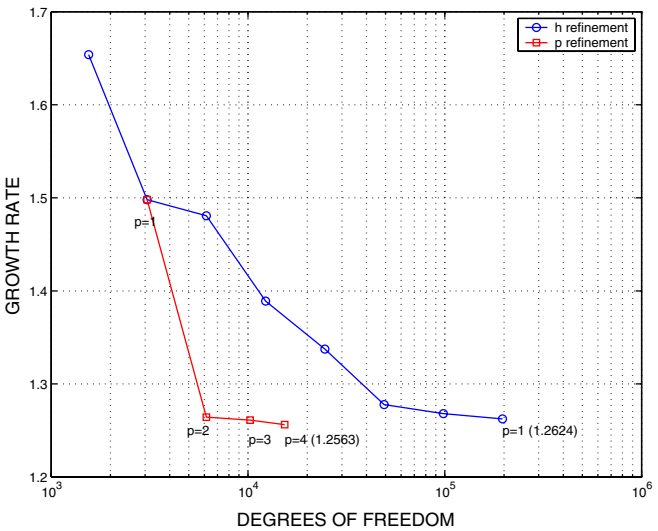

Fig. 7. Growth rates with h- and p-refinement for $\epsilon = 2.0e^{-2}$.

$$\begin{aligned}\Omega(\ ,\kappa_{\searrow}) &= \phi(\ ,\kappa_{\searrow}) = 0,\\ \psi(\ ,\kappa_{\searrow}) &= \psi_0.\end{aligned} \tag{6.4}$$

A viscosity of $\mu = 0.005$ was used in all simulations.

6.1. Non-adaptive computation

We first present results of a simulation with polynomial degree $p = 1$ on a fixed mesh of 32,768 triangles of the type shown in Fig. 2 with $N_s = 128$. The initial perturbation magnitude is $\epsilon = 1.0\text{e}^{-4}$. The magnetic flux, shown in Fig. 3 indicate that the vortices distort as they turn and line up. The velocity and vorticity, also shown in Fig. 3, indicate that the motion of the instability is a combination of rotation of the vortices about the origin and displacement of vortices relative to each other. As the vortices turn, oppositely directed magnetic field lines intersect at the leading edges of the vortices. This phenomenon is known as magnetic recon-

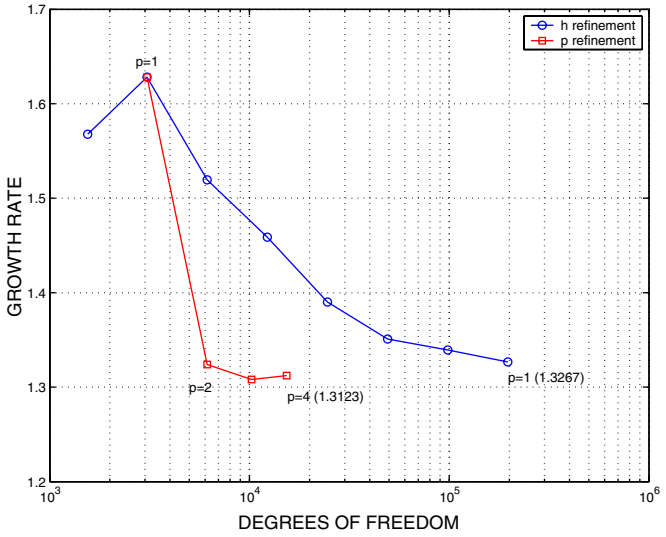

Fig. 8. Growth rates with h- and p-refinement for $\epsilon = 1.0\text{e}^{-3}$.

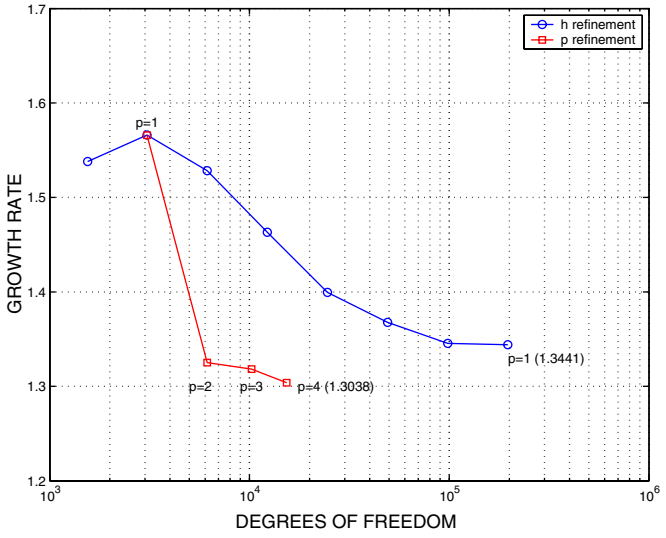

Fig. 9. Growth rates with h- and p-refinement for $\epsilon = 1.0\text{e}^{-4}$.

nection and is not permitted in ideal MHD. It occurs due to insufficient spatial resolution. A consequence of this is the poor resolution of current sheets as shown in the lower right of Fig. 4. This is also reflected in the value of peak current density (56) when the two vortices line up horizontally (see Fig. 5). The peak current is

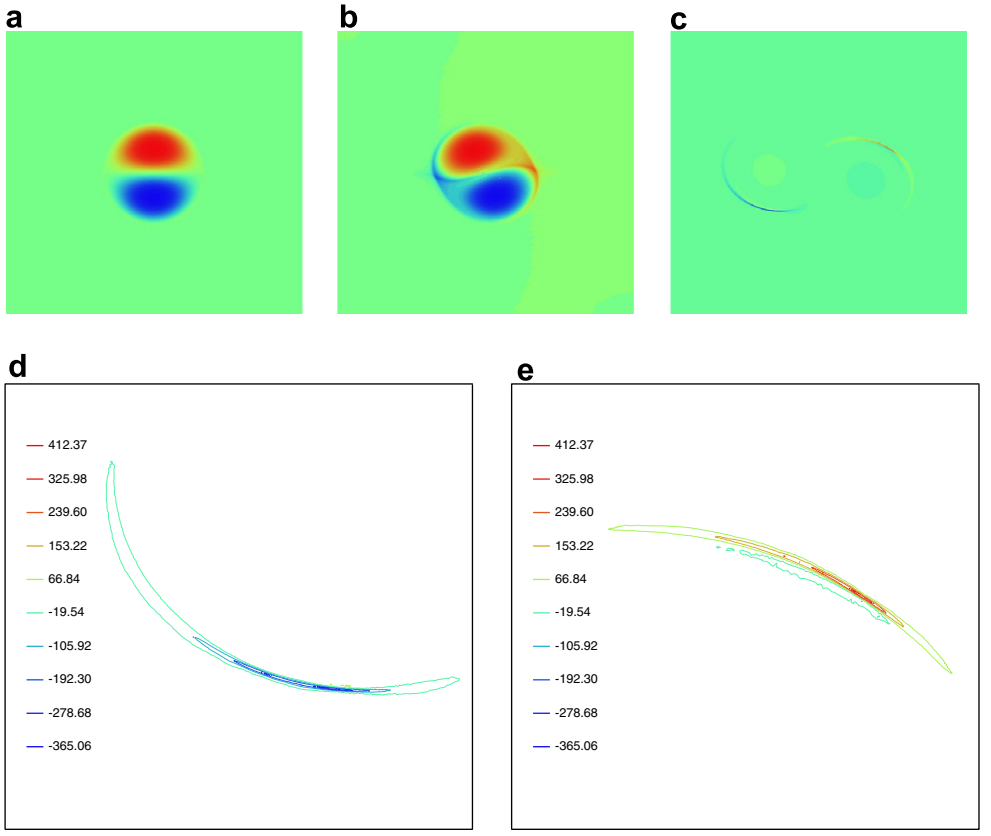

Fig. 10. Current density (top) and current sheets (bottom) when using the Z^2 error estimator with $\eta_{tol} = 0.01$ and $p = 1$. Current (C): (a) $t = 0.0$, (b) $t = 6.0$, (c) $t = 7.3$. (d) and (e) Current sheets.

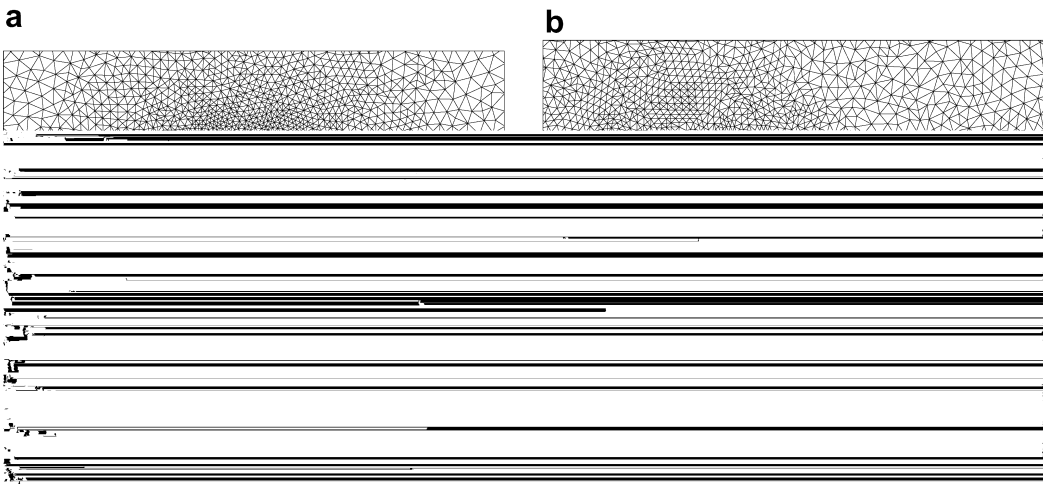

Fig. 11. Meshes at $t = 0$ and $t = 7.3$ when using Z^2 error estimator with $\eta_{tol} = 0.01$ and $p = 1$. (a) Initial mesh of 29,526 triangles. (b) Adapted mesh of 37,981 triangles at $t = 7.3$.

only about five times its initial value whereas nearly singular values are expected in the case of ideal MHD. Better resolution of the current sheets would result in a much higher peak current density.

Better resolution of the current sheets can be done by adaptive procedures that automatically refine the mesh in order to control the discretization errors.

6.2. Growth rates

Like the current sheets, another quantity of interest is the linear growth rate of the instability. The linear growth rate γ is the slope of the linear portion of the logarithm of the kinetic energy as a function of time. The slope is determined by a least squares fit of a linear polynomial as shown in Fig. 6. A growth rate of $\gamma = 1.3455$ was obtained for the simulation of Section 6.1.

We did a systematic study of the effect of uniform h- and p-refinement on growth rates. For the h-refinement study, uniform meshes of the type shown in Fig. 2 with $N_s = 16, 23, 32, 45, 64, 90, 128$ and 181 were used. For the p-refinement study, polynomial degrees $p = 1$–4 were used on a mesh with $N_s = 23$. Figs. 7–9 show the growth rates as a function of the logarithm of the number of degrees of freedom obtained with h- and p-refinement for different magnitudes of the initial perturbation ϵ. The number of degrees of freedom for only the magnetic variable have been used. We notice a slight dependence of the growth rate on the magnitude of the initial perturbation, but, in all cases, there is a more rapid convergence of growth rates with p-refinement than with h-refinement. However, we note a slight difference in converged values from h- and p-refinement particularly for the case with $\epsilon = 1.0e^{-4}$. This may be attributed to low order methods failing to converge in some cases. In general, there is a clear advantage of the higher-order methods with respect to growth rate computation both in terms of accuracy and efficiency.

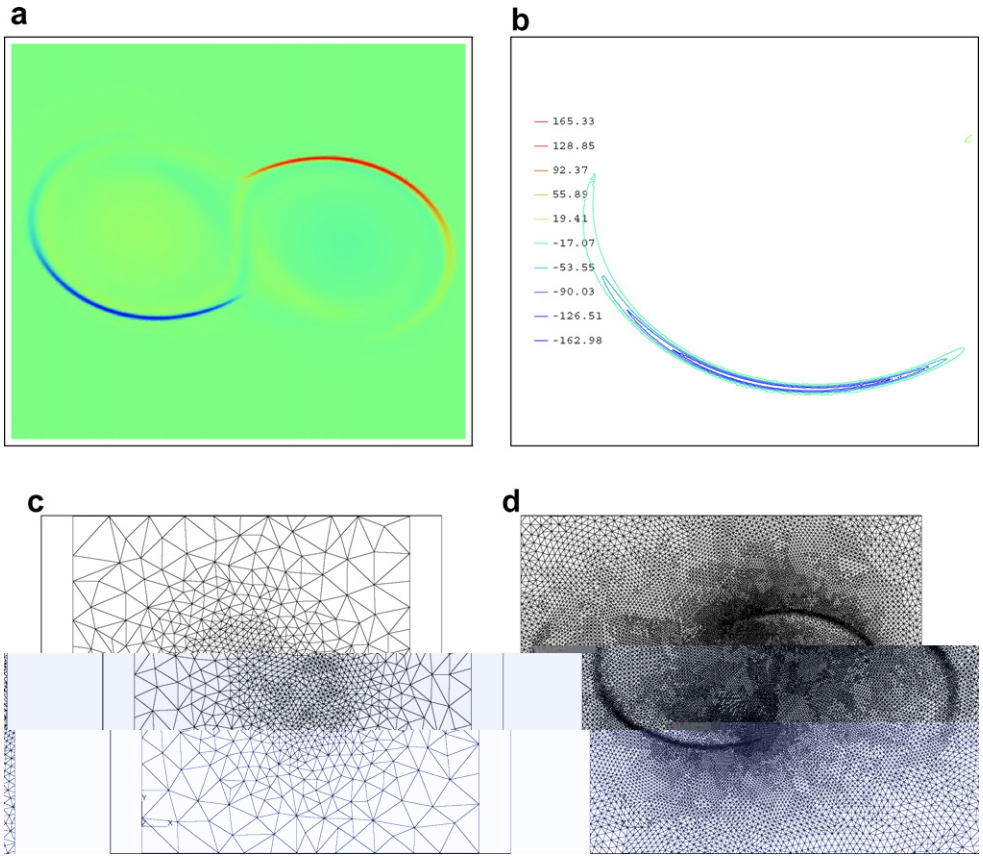

Fig. 12. Current density (top) and adapted meshes at $t = 0$ and $t = 8.5$ using the order extrapolation estimate with $\eta_{tol} = 0.02$ and $p = 1$. (a) Current density. (b) Current sheets. (c) Initial mesh of 1843 triangles. (d) Adapted mesh of 56,009 triangles at $t = 7.7$.

6.3. Adaptive computation

Adaptive solutions were obtained using the error estimation and mesh adaptivity procedures described in Section 5. A posteriori spatial error estimates of the magnetic field was used to adapt the mesh at the end of every time step. The corresponding flux function is

$$\sigma(\psi_{,\eta}) = \left[\frac{\partial\psi_{,\eta}}{\partial x}, -\frac{\partial\psi_{,\eta}}{\partial}\right].$$

The justification for using this flux function is that the current sheets form at the intersection of oppositely directed magnetic field lines. Better resolution of the magnetic field will result in better resolution of current sheets.

The time step for integration was chosen such that the local temporal discretization error in the magnetic flux (ψ) was one-tenth ($\alpha = 0.1$) in Eq. (5.6) of the global spatial discretization error. Temporal discretization errors in all the other variables were ignored. All the simulations were started with an initial timestep of 0.0025. The timestep during the simulations was observed to vary within an order of magnitude of the initial timestep. The global spatial error tolerance η_{tol} is a problem dependent parameter and, as such, is difficult to determine. We used numerical experimentation to arrive at an appropriate value. The adaptive simulations were done on unstructured triangular meshes and the initial mesh was adapted to the spatial discretization error in the initial magnetic field. We will mainly compare results from adaptive simulations in terms of resolution of the current sheets when the magnetic vortices line up horizontally.

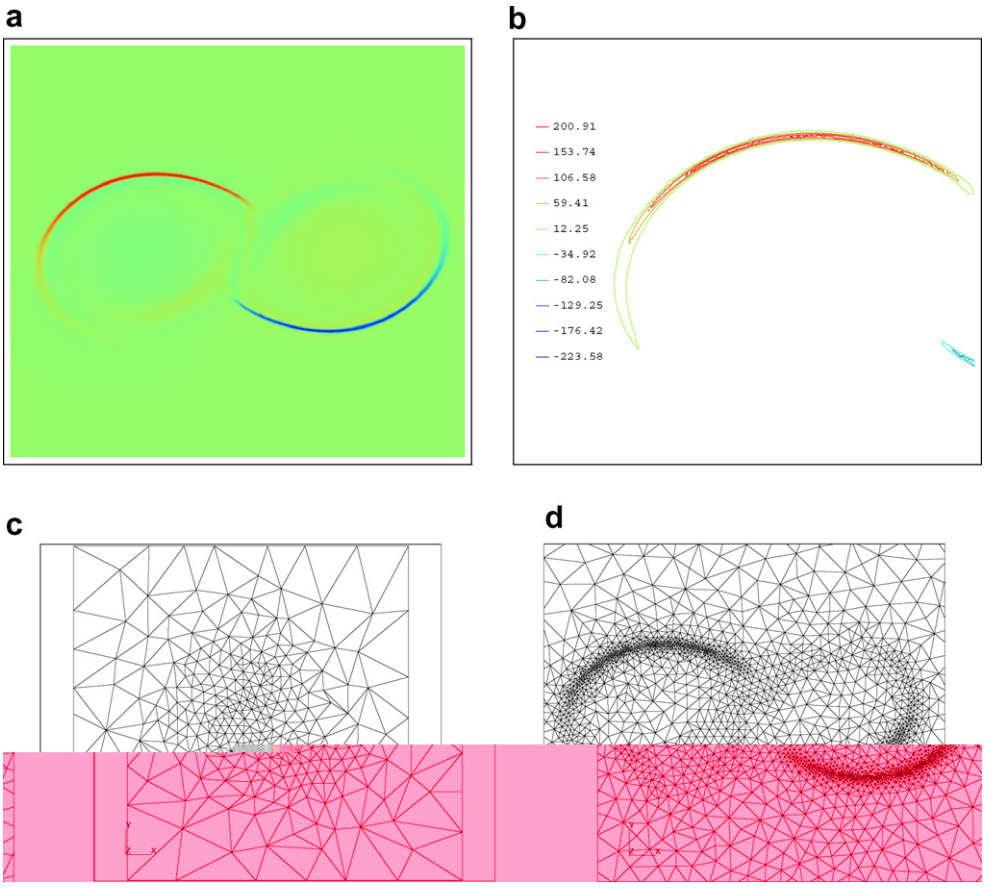

Fig. 13. Current density (top) and adapted meshes at $t = 0$ and $t = 6.3$ using order extrapolation estimate with $\eta_{\text{tol}} = 0.005$ and $p = 2$. (a) Current density. (b) Current sheets. (c) Initial mesh of 1843 triangles. (d) Adapted mesh of 6035 triangles at $t = 6.3$.

Fig. 10 shows results obtained using the Z^2 estimator with $\eta_{tol} = 0.01$. Close up views of the current (Fig. 10(d) and (e)) indicate that the current sheets have been resolved. Some meshes are shown in Fig. 11. The growth rate of the kinetic energy was $\gamma = 1.3344$.

Fig. 12 shows results obtained using the order extrapolation error estimate with $\eta_{tol} = 0.02$. The current sheets in Fig. 12(d) are much better resolved than those obtained using the Z^2 estimator in Fig. 10. In this case, the final adapted mesh had 56,009 elements and the growth rate was $\gamma = 1.3027$. Since, we propagate the higher-order solution when using extrapolation error estimates, the solution obtained using the order extrapolation is of spatial order two.

Fig. 13 shows results obtained using order extrapolation estimator with $p = 2$ and $\eta_{tol} = 0.005$. The propagated solution has degree three and the adapted mesh has 6035 elements. The current sheets are better resolved when compared to the degree one solution in Fig. 10. The growth rate of the kinetic energy was found to be $\gamma = 1.3357$. Both the higher-order solutions give better resolution of current sheets when compared to the linear solution, thus, demonstrating a benefit of higher-order methods.

Current sheets from additional adaptive computations using different error estimates and error tolerances are shown in Fig. 14. In general, for a given error tolerance, $p = 2$ solution is better resolved than the $p = 1$ solution. To see this, compare the current sheets obtained with $\eta_{tol} = 0.01$ in Fig. 10(e) ($p = 1$) and Fig. 12(b) ($p = 2$). However, a $p = 3$ solution of comparable resolution requires specification of a much lower tolerance (see Fig. 13(b) with $\eta_{tol} = 0.005$).

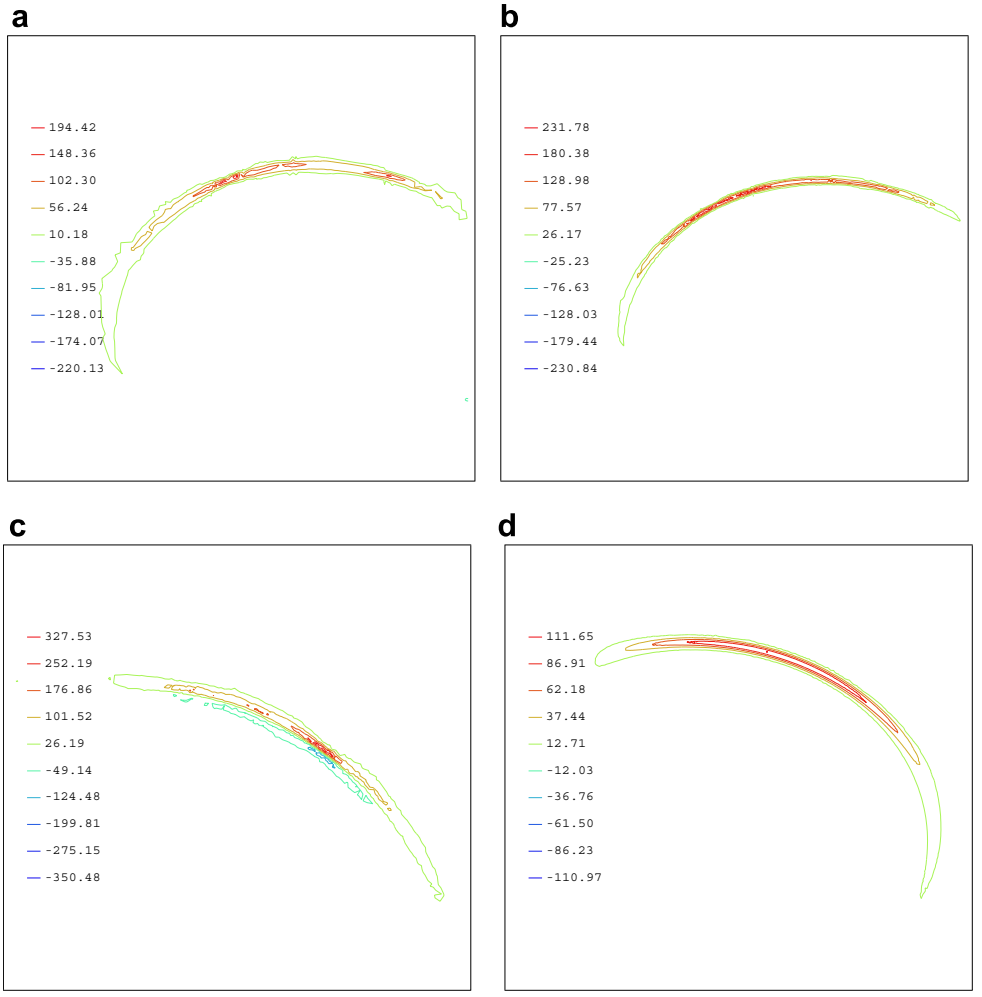

Fig. 14. Current densities obtained by various adaptive computations: (a) $p = 3$, $\eta_{tol} = 0.02$, 1732 elements, (b) $p = 3$, $\eta_{tol} = 0.01$, 5186 elements, (c) $p = 1$, $\eta_{tol} = 0.02$, 11,241 elements, (d) $p = 2$, $\eta_{tol} = 0.01$, 76,094 elements.

In Figs. 15–17, we compare the peak current densities, number of elements and total energies from various adaptive computations with a standard (non-adaptive) computation. As anticipated, adaptive computations result in higher values of peak current densities. Peak current densities obtained from adapted $p = 1$ solutions are significantly higher than those from adapted higher order solutions. Additionally, the peak current density from an order 3 adaptive simulation is higher than that from a order 2 solution. However, higher peak current density do not necessarily correspond to better resolution of current sheets. To see this, compare the current sheets obtained using higher-order method (Figs. 12 and 13) with those obtained with $p = 1$ (Fig. 10).

The Figs. 15–17 also indicate that the time at which the current densities begin their exponential growth varies for different simulations. The exponential growth starts to occur after the two vortices have turned from their initial horizontal position somewhere inbetween the horizontal and vertical position. All our numerical experiments indicated a sensitive dependence of the instability to initial conditions. Slightly different initial conditions brought about by the mapping of the initial magnetic field onto the mesh with different orders resulted in the instability turning at different times. However, once the current sheets begin to form, our adaptive procedure works as anticipated.

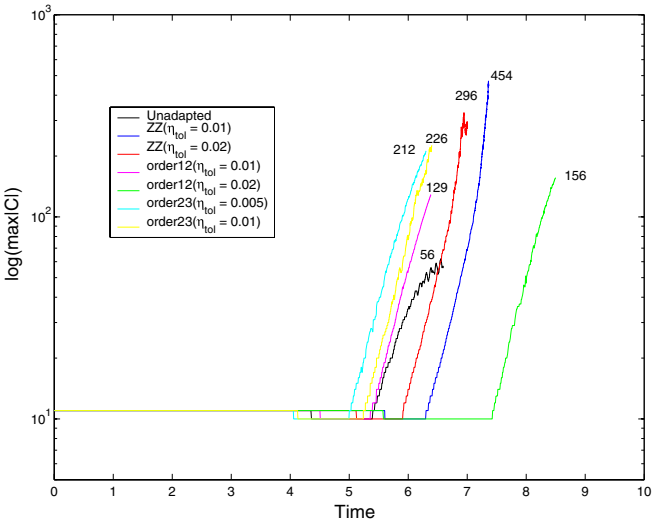

Fig. 15. Peak currents as function of time for an unadapted and various adaptive computations.

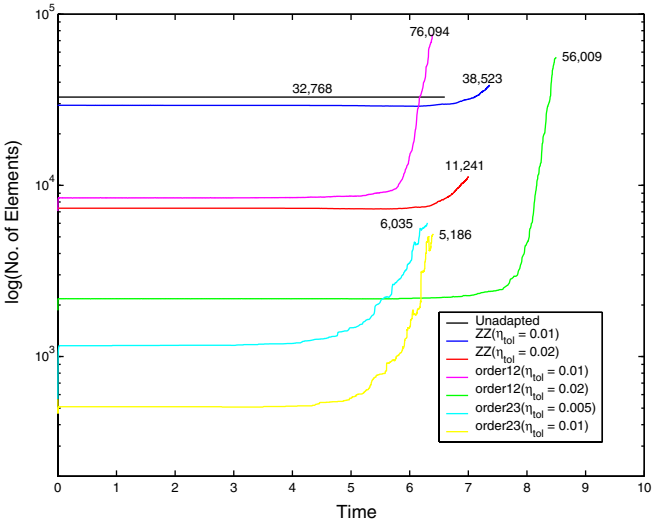

Fig. 16. Number of elements as a function of time for an unadapted and various adaptive computations.

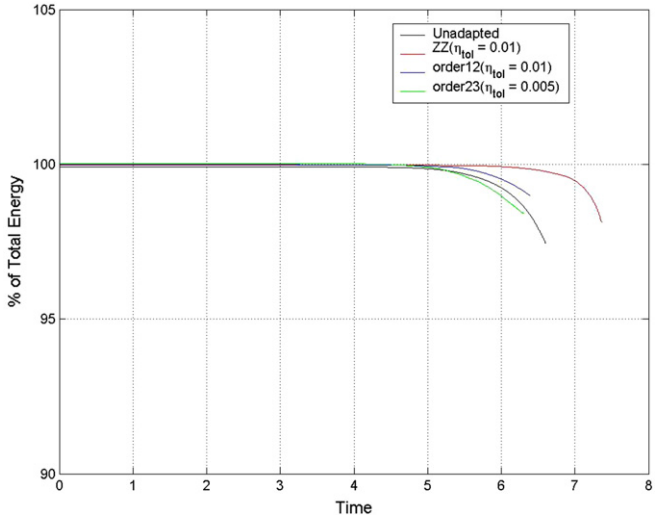

Fig. 17. Total energy as a function of time for an unadapted and various adaptive computations.

Fig. 16 shows that the growth in the number of elements used for a computation keeps pace with the exponential growth of peak current density. The total energy plots in Fig. 10 show that the energy is conserved better (less than 2% loss) for the all the adaptive simulations. The unadapted simulation shows a greater loss of energy due to numerical reconnection.

Finally, Strauss et al. [1] obtained $\gamma = 1.2$ in adaptive simulations with linear elements and Richard et al. [26] obtained a growth rates in the range of $1.3 < \gamma < 1.4$, depending on pressure for compressible MHD with resistivity. We obtained growth rates in the range of $1.25 < \gamma < 1.34$ in our simulations.

7. Summary and conclusions

We describe an adaptive finite element procedure for solving incompressible magnetohydrodynamic flow problems in stream function-vorticity form. The procedure uses a stabilized finite element formulation and adaptive *h*-refinement based on a posteriori temporal and spatial error estimates of the magnetic field. The methods were applied to study a tilt instability under ideal magnetohydrodynamics conditions. A systematic study of the linear growth rate of the tilt instability with respect to *h*- and *p*-refinement was conducted and results were obtained using different spatial error estimators. Our results indicate that higher-order methods provide higher solution accuracy per unit computation for growth rates. In addition, they provide for better resolution of current sheets.

In this work, we applied relatively standard a posteriori error estimation techniques to adaptively solve equations that model single fluid ideal magnetohydrodynamics. Work is underway to develop better error estimation techniques and extend them to adaptively solve two-fluid models of magnetohydrodynamics.

References

[1] H.R. Strauss, D.W. Longcope, An adaptive finite element method for magnetohydrodynamics, J. Comput. Phys. 147 (1998) 318–336.
[2] D.W. Longcope, H.R. Strauss, The coalescence instability and the development of current sheets in two-dimensional magnetohydrodynamics, Phys. Fluids B 8 (1993) 2858–2869.
[3] D.D. Schnack, I. Lottati, Z. Mikic, P. Satyanarayana, A finite-volume algorithm for three dimensional magnetohydrodynamics on an unstructured, adaptive grid in axially symmetric geometry, J. Comput. Phys. 140 (1998) 71–121.
[4] W. Park, D.A. Monticello, R.B. White, S.C. Jardin, Nonlinear saturation of the internal kink mode, Nucl. Fusion 20 (9) (1980) 1181–1185.
[5] H. Friedal, R. Grauer, C. Marliani, Adaptive mesh refinement for singular current sheets in incompressible magnetohydrodynamic flows, J. Comput. Phys. 134 (1997) 190–198.
[6] S.C. Jardin, A triangular finite element with first-derivative continuity applied to fusion MHD applications, J. Comput. Phys. 200 (2004) 133.

[7] J.E. Flaherty, P.K. Moore, Integrated space–time adaptive *hp*-refinement methods for parabolic systems, Appl. Numer. Math. 16 (1995) 317–341.
[8] A.N. Brooks, T.J.R. Hughes, Streamline upwind/Petrov–Galerkin formulations for convection dominated flows with particular emphasis on the incompressible Navier–Stokes equations, Comp. Meth. Appl. Mech. Eng. 32 (1982) 199–259.
[9] T.J.R. Hughes, A. Brooks, A theoretical framework for Petrov–Galerkin methods with discontinuous weighting functions: application to the streamline upwind procedure, Finite Elements in Fluids, vol. 4, Wiley, 1982, pp. 47–65.
[10] S. Adjerid, M. Aiffa, J.E. Flaherty, High-order finite element methods for singularly perturbed elliptic and parabolic problems, SIAM J. Appl. Math. 55 (2) (1995) 520–543.
[11] S. Adjerid, M. Aiffa, J.E. Flaherty, Computational methods for singularly perturbed systems, Proc. Symp. Appl. Math. 56 (1999) 47–83.
[12] T.J.R. Hughes, A simple scheme for developing 'upwind' finite elements, Int. J. Numer. Meth. Eng. 12 (1978) 1359–1365.
[13] T.J.R. Hughes, L.P. Franca, G.M. Hulbert, A new finite element formulation for computational fluid dynamics: VIII. The Galerkin/least-squares method for advective-diffusive equations, Comp. Meth. Appl. Mech. Eng. 73 (1989) 173–189.
[14] T.E. Tezduyar, Y. Osawa, Finite element stabilization parameters computed from element matrices and vectors, Comp. Meth. Appl. Mech. Eng. 190 (2000) 411–430.
[15] L.P. Franca, S.L. Frey, T.J.R. Hughes, Stabilized finite element methods: I. Application to the advective-diffusive model, Comp. Meth. Appl. Mech. Eng. 95 (1992) 253–276.
[16] P.G. Ciarlet, The Finite Element Method for Elliptic Problems, North-Holland, Amsterdam, 1978.
[17] G.K. Batchelor, An Introduction to Fluid Dynamics, Cambridge University Press, 1967.
[18] B. Szabo, I. Babuska, Finite Element Analysis, Wiley, 1991.
[19] D. Halliday, R. Resnick, J. Walker, Fundamentals of Physics, Wiley, 1997.
[20] I. Harari, T.J.R. Hughes, What are C and h?: inequalities for the analysis and design of finite element methods, Comp. Meth. Appl. Mech. Eng. 97 (1992) 157–192.
[21] M. Ainsworth, J.T. Oden, A Posteriori Error Estimation in Finite Element Analysis, Wiley, 2000.
[22] I. Babuska, T. Strouboulis, The Finite Element Method and its Reliability, Oxford Science Publications, 2001.
[23] O.C. Zienkiewicz, J.Z. Zhu, The Superconvergent Patch Recovery and A Posteriori Error Estimates. Part I: The Recovery Technique, Int. J. Numer. Meth. Eng. 33 (1992) 1331–1364.
[24] E. Hairer, S.P. Norsett, G. Wanner, Solving Ordinary Differential Equations I: Nonstiff Problems, Springer Verlag, Berlin, 1987.
[25] M. Braack, R. Becker, R. Rannacher, J. Warnatz, An adaptive finite element method for combustion problems, in: Third Summer Conference, Numerical Modeling in Continuum Mechanics, Charles University, Prague, 1997.
[26] R.L. Richard, R.D. Sydora, M. Ashour-Abdalla, Magnetic reconnection driven by current repulsion, Phys. Fluids B 2 (3) (1990) 488–494.
[27] M.W. Beall, M.S. Shephard, An object-oriented framework for reliable numerical simulations, Eng. Comput. 15 (1999) 61–72.
[28] X. Li, M.S. Shephard, M.W. Beall, 3D anisotropic mesh adaptation using mesh modifications, Comp. Meth. Appl. Mech. Eng. 194 (2005) 4915–4950.
[29] J.F. Remacle, X. Li, M.S. Shephard, J.E. Flaherty, Anisotropic adaptive simulations of transient flows using discontinuous Galerkin methods, Int. J. Numer. Meth. Eng. 62 (2005) 899–923.